Precipitation on the Manus Island of Papua New Guinea and ice cloud radiative effects in the surrounding atmosphere in boreal winters

Tong Ren,[a] Ping Yang,[a]

Norman G. Loeb,[b] William L. Smith Jr.,[b] Patrick Minnis[c,b]

[a]*Department of Atmospheric Sciences, Texas A&M University, College Station, Texas*

[b]*NASA Langley Research Center, Hampton, Virginia*

[c]*Analytical Mechanics Associates, Inc., Hampton, Virginia*

Corresponding author: Tong Ren, tr7585@tamu.edu

ABSTRACT

The longwave cloud radiative effect (LW CRE) plays a critical role in regulating tropical moist convection by modifying the atmospheric energy budget. While previous studies have linked LW CRE to the maintenance of convective quasi-equilibrium (CQE) on large scales, its influence at shorter timescales and on individual convective events remains less explored. In this study, we analyze the relationship between precipitation and LW CRE on daily timescales at a location over the equatorial western Pacific. We focus on how LW CRE shapes the thermodynamic environment prior to deep convection. The present results show that enhanced LW CRE and surface turbulent heat fluxes act to increase atmospheric moist static energy (MSE) before rainfall events, supporting conditions favorable for deep convection. Notably, LW CRE may facilitate ice sublimation in the lower portions of ice clouds by enhancing radiative warming, thereby contributing to the preconditioning of the atmospheric column. In addition, increased humidity in the lower free troposphere above the planetary boundary layer (PBL) is found to reduce the height of anvil cloud tops, suggesting a modulation of convective vertical structure by pre-convective moisture. These findings provide a process-level perspective on how LW CRE contributes to maintaining a quasi-equilibrium convective state in the tropics.

1. Introduction

The conservation of the column-integrated moist state energy (MSE) is often used to study moist convection (Neelin and Held 1987). Cloud radiative forcing (Ramanathan 1987) or effect (CRE), a source term of the MSE budget, has been found to affect the tropical rainfall distribution (Lau et al. 2020; Medeiros et al. 2021; Zhang et al. 2021b) and associated atmospheric circulations (Raymond 2000; Sherwood et al. 1994; Slingo and Slingo 1988, 1991; Tian and Ramanathan 2002, 2003) at sub-seasonal and longer timescales (Benedict et al. 2020; Middlemas et al. 2019). In the longwave (LW) spectral regime, clouds absorb surface emitted radiation and re-emit at a cooler atmospheric temperature, placing a greenhouse effect on the atmosphere and the surface. The temperature difference between high-level ice clouds and the surface is larger than that between low-level clouds and the surface. Consequently, high-level ice

clouds have a stronger LW CRE than low-level clouds at the top of the atmosphere (TOA). Global enhancement of LW CRE in an atmosphere-only general circulation model (GCM) shifts the midlatitude jet poleward in the Southern Hemisphere and enhances the Walker circulation (Gu et al. 2021). Strong events of the tropical intraseasonal oscillation—Madden-Julian Oscillation (MJO) are associated with strong radiative heating of the atmosphere, which is thought to facilitate the passage of MJO over the Maritime Continent (Zhang et al. 2019). When atmospheric radiative heating is horizontally homogenized on a rotating cloud-permitting sea water-covered planet with constant sea surface temperature (SST), the slow-moving MJO-like moisture modes become fast-travelling Kelvin-like ones (Khairoutdinov and Emanuel 2018). Synoptic-scale radiative heating/cooling distributions within both the planetary boundary layer (PBL) and the free atmosphere affect the tropical cyclone frequency in global model simulations (Zhang et al. 2021a, 2023).

Despite the LW CRE enhancement of storms over tropical oceans, LW CRE produces a different influence in the midlatitudes (Schäfer and Voigt 2018). Suppression of radiative interactions in a GCM tends to cool and heat the warm and cold sectors of a midlatitude cyclone, respectively, resulting in reduced near-surface and tropopause eddy available potential energy in the midlatitudes and enhanced extratropical eddy kinetic energy (Mischell et al. 2024). The respective enhancement and weakening of storms over tropical oceans and midlatitudes by LW CRE may be reconciled when the tropical deep convection over oceans occurs in a convective quasi-equilibrium (CQE) regime (Emanuel 2023; Yano and Plant 2012). Under the CQE, cumulus convection kinetic energy generated primarily by the buoyancy force is totally dissipated via momentum entrainment through cloud boundaries and by the frictional drag that falling hydrometeors put on cumulus updrafts (Arakawa and Schubert 1974; Lord and Arakawa 1980). The CQE conditions in deep convective regimes over the tropics are supported by sounding data, which suggest that the buoyancy of an air parcel uplifted adiabatically from the sub-cloud layer to 300 hPa is indistinguishable from zero when the generated condensate is loaded within the air parcel (Xu and Emanuel 1989). Based on observations, Jakob et al. (2019) show that on daily scales and longer, the entire tropics is near radiative-convective equilibrium (RCE) (Held et al. 1993), which is an idealized realization of CQE (Yano and Plant 2012). In the

aquaplanet configuration of GCMs where the planet surface is completely covered by water (Medeiros et al. 2016), the deactivation of LW CRE significantly weakens and widens the tropical rain belt (Medeiros et al. 2021). In both the standard and aquaplanet configurations of GCMs, the removal of LW CRE reduces tropical precipitation extremes (Medeiros et al. 2021).

While the suppression of LW CRE has a significant effect on model precipitation simulations, the correlation between observed CRE and precipitation varies across the tropics (Jakob et al. 2019). Satellite observation-based estimates show that the ratio of monthly mean cloud radiative heating of the atmosphere to precipitation latent heating within every 2.5º × 2.5º gridbox ranges from 0 to 1.5 over the tropics where deep convective systems prevail (Daloz et al. 2018). The ratio of instantaneous cloud atmospheric radiative heating to latent heating varies over a wider range, even if the lightest precipitation cases (precipitation rate < 0.01 mm h^{-1}) are excluded (Sun et al. 2022). Based on reanalysis data, daily averaged diabatic heating increases with decreasing OLR over the tropical western Pacific at 400 hPa (Zhang et al. 2017). In addition, surface turbulent heat flux—another source term of atmospheric MSE—increases with rising SST, which is well known to regulate tropical deep convection and precipitation (Graham and Barnett 1987). In the west Pacific, when monthly mean SST exceeds 28ºC, deep convective clouds are enhanced (Fu et al. 1990). Across the entire tropics, the monthly mean OLR decreases significantly as SST increases from 26ºC to approximately 29.5º-30ºC. At temperatures exceeding 30ºC, OLR increases as SST continues to rise (Zhang 1993). Over the tropical oceans, as SST increases from 27 to 30ºC, organized deep convective systems become more frequent, contributing more to total precipitation and increasing the ratio of LW cloud radiative heating to latent heating in the troposphere (Hsiao et al. 2024).

The features of deep convective clouds change in response to surface turbulent heat flux variations, which in turn shape the radiative heating of the atmosphere and hence the local rate of atmospheric MSE change. Fu et al. (1990) showed that the top height of deep convective clouds generally increases with increasing SST over the west Pacific. Fu et al. (1990) explained the observed correlation between SST and cloud top height with the CQE perspective: As SST increases, the presumably moistened PBL nurtures cumulus convection kinetic energy, which can

be balanced by in-cloud dissipations only if cloud top height also increases (Lord and Arakawa 1980). Numerous studies have successfully linked the MSE sources and sinks to tropical moist convection in the context of some kind of quasi-equilibrium. To the best of our knowledge, however, few studies have focused on understanding how processes operating at short time scales cause the tropical convective environment to reach a quasi-equilibrium state, which is necessary for applying existing CQE theories. Fu et al. (1994) is a seminal example of a study that approaches tropical deep convection from a process-level perspective, linking SST-driven variations in surface fluxes and atmospheric humidity to changes in convective structure and depth. In the present study, we show that there is only a weak correlation between precipitation and LW CRE on rainy days at the daily scale over a location in the equatorial western Pacific. However, we find that LW CRE has a significant influence on the thermodynamic conditions prior to the onset of moist convection, thereby helping to elucidate the role of LW CRE in CQE over tropical oceans from a process-level perspective. Section 2 introduces the data and methods we use. The results are presented in Section 3, followed by the conclusions in Section 4.

2. Data and methods

The Atmospheric Radiation Measurement (ARM) Program of the United States Department of Energy (DOE) has a site on the Manus Island, Papua New Guinea (PNG) (2.060ºS, 147.425ºE), from which the interpolated radiosonde (INTERPOLATEDSONDE) data (Jensen et al. 2001) and the surface rain gauge measurement (Surface Meteorological Instrumentation) data (Kyrouac et al. 1997) are adopted for this study. The altitude of this site is 4 m. We choose to analyze the data from the two El Niño boreal winters (2006–2007 and 2009–2010) and the two La Niña boreal winters (2007–2008 and 2010–2011) as identified in Takahashi et al. (2024), allowing us to compare our point-based results with the deep convection feature statistics reported for the entire tropics in that study during the same period. We summed rainfall measured by the tipping bucket rain gauge (TBRG) on each day to get the daily accumulated rainfall. We averaged the 1-min interpolated radiosonde data on each day to get the vertical profiles of daily mean temperature and specific humidity. The daily mean temperature and specific humidity vertical profiles were subsequently smoothed with a 20 hPa-window running mean before they were used

to compute the MSE vertical profile. The gridded hourly SST data from the European Center for Medium-Range Weather Forecasts (ECMWF) Reanalysis, version 5 (ERA5) (Hersbach et al. 2023) were averaged over a 2º-by-2º domain centered at the ARM site. Subsequently, the domain-mean hourly SST data on each day were averaged to obtain the daily mean SST time series. The surface of the 2°-by-2° domain consists primarily of sea water. The ERA5 SST data, with a spatial resolution of 0.25° × 0.25°, corresponds to a 9 × 9 grid of data points within the study domain. Two out of the 9 × 9 grid boxes represent the Manus Island, surrounded by the remaining oceanic grid boxes.

The Clouds and Earth's Radiant Energy System (CERES) synoptic TOA and surface fluxes and clouds (SYN1deg) product provides hourly 1° × 1° observed clear-sky and all-sky LW broadband radiation fluxes data at the TOA (Doelling et al. 2013, 2016). The difference between clear-sky and all sky LW radiation fluxes is the LW CRE. Hereinafter, we omit TOA and refer LW CRE to LW CRE at the TOA. We averaged CERES SYN1deg observed LW CRE over the 2º-by-2º domain centered at the ARM site to get the hourly domain-mean LW CRE. Based on hourly LW CREs, we computed daily mean and daily maximum LW CREs.

The CERES SYN1deg product also provides retrieved cloud properties (Minnis et al. 2021, 2023; Trepte et al., 2019). CERES cloud retrievals have been frequently used to study convection features (Wall et al. 2018; Xu et al. 2005, 2007, 2019). In the CERES cloud retrieval algorithm, clouds are categorized into high (p_e < 300 hPa), upper-middle (300 < p_e < 500 hPa), low-middle (500 < p_e < 700 hPa), and low (700 < p_e < 1000 hPa) clouds, where p_e is the pressure at which atmospheric temperature equals to the cloud effective radiating temperature. The SYN1deg product provides retrieved cloud properties, including cloud phase, fraction, water path, and effective radius, for each of the 4 cloud height categories. High clouds are almost always identified as ice clouds. Upper-middle clouds are frequently identified as either ice or liquid clouds. Liquid clouds predominantly prevail in the lower two categories. We averaged the product of cloud fraction and ice water path (IWP) for each ice phase categories over the domain to get hourly ice-phase-pixel-mean IWPs in the 4 cloud height categories, respectively. Hourly ice-phase-pixel-mean IWPs in the high and upper middle category were summed and then used

to compute daily mean and daily maximum IWPs. In a similar way, we computed hourly cloud fraction-weighted mean high ice cloud top temperature (CTT) over the domain and then averaged the hourly data on the same day to obtain daily mean high ice CTT time series. It should be noted that IWP represents an estimate of the total condensate (liquid plus ice water path) for multilayered ice-over-water clouds. Such clouds are not explicitly identified in the CERES cloud retrievals. During the daytime, ~22% of the clouds identified as ice phase comprise ice-over-water systems (Sun-Mack et al. 2024).

The passive-sensor cloud retrievals do not provide much information about the hydrometeor layering within the clouds. To address that shortcoming, we employ the 2C-ICE product (Deng et al., 2010, 2013, 2015). It provides IWC vertical profiles retrieved along a narrow field of view (FOV) track of the CloudSat Cloud Profiling Radar (CPR; Tanelli et al. 2008) and Cloud-Aerosol Lidar and Infrared Pathfinder Satellite Observations (CALIPSO; Winker et al. 2010) Cloud-Aerosol LIdar with Orthogonal Polarization (CALIOP). Those two satellites take measurements within a few minutes of the coincident Aqua MODIS data used in the CERES cloud retrievals. The 2C-ICE algorithm links the CPR radar reflectivity factor and CALIOP lidar backscattering signal to IWC and ice cloud effective radius via radar and lidar equations. It assumes a modified gamma size distribution of ice particles with several different shapes whose optical properties at the radar and lidar wavelengths are taken from Hong (2007) and Yang et al. (2000). The CPR FOV has cross-track and along-track resolutions of 1.4 and 1.7 km, respectively. We selected the 2C-ICE granules that have ice-cloud-containing FOVs within the 2º-by-2º domain during the 4 winter periods. The pressure levels and the corresponding temperatures for each 2C-ICE retrieval column were obtained from radiosonde data recorded at the minute the study domain was scanned by CPR and CALIOP. The averaging was performed at the same pressure level. Only the columns in which ice clouds were detected above 300 hPa, but not below, were included in the averaging. The temperature at the level where the mean IWC peaked above 300 hPa is defined as cloud maximum mass temperature (CMMT).

We first analyze the correlations between precipitation and SST, and between precipitation and LW CRE on the rainy days. Next, all the non-rainy days followed by rain days were identified

and used to determine the correlations between LW CRE on non-rainy days and precipitation on following rainy days. We then examined how LW CRE correlates with MSEs in different atmospheric layers and convective available potential energy (CAPE) on non-rainy days. Additionally, we study how MSEs in different atmospheric layers and CAPE correlate with precipitation during the following rainy days. Because CTT is important to measure the high ice cloud greenhouse effect, we also correlated MSEs in different atmospheric layers and CAPE on non-rainy days with CERES SYN1deg daily mean high ice CTT on following rainy days.

Finally, we compare the CERES high ice CTT with the 2C-ICE CMMT above 300 hPa. This comparison utilizes the CERES SYN1deg cloud fraction-weighted high ice CTT corresponding to the hour when the study domain was scanned by the CPR and CALIOP. If no high ice clouds were identified by the CERES cloud retrieval algorithm during the relevant hour, the mean of the ice CTTs from the preceding and following hours is used instead.

3. Results and Discussion

a. Correlations between precipitation and LW CRE

In the study area, the El Niño winters are wetter than the La Niña winters in term of precipitation (Table 1), while the mean SSTs in the selected two El Niño winters and two La Niña winters differ by only 0.3 K. Table 1 reveals that, while the mean daily averaged and daily maximum LW CREs on rainy days are close in the El Niño and La Niña winters, mean daily averaged and daily maximum LW CREs during the El Niño winter period exceed their La Niña counterparts. Mean daily averaged and maximum ice-phase-pixel-mean IWPs are larger during the El Niño than during the La Niña on rainy days and throughout, but the differences in mean IWPs between the El Niño and the La Niña are larger throughout than on rainy days. The results suggest that the non-rainy days have more ice clouds and a stronger LW CRE during the El Niño than during the La Niña.

Variables	El Niño	La Niña
Mean SST (K)	302.68	302.99
Number of rainy days	140	102

Mean daily accumulated rainfall (mm)	9.41	6.04
Mean daily accumulated rainfall on rainy days (mm)	12.10	10.72
Mean daily averaged domain-mean LW CRE (W m^{-2})	69.00	60.40
Mean daily averaged domain-mean LW CRE on rainy days (W m^{-2})	74.96	75.38
Mean daily averaged ice-phase-pixel-mean IWP (g m^{-2})	110.84	68.76
Mean daily averaged ice-phase-pixel-mean IWP on rainy days (g m^{-2})	129.29	102.07
Mean daily maximum domain-mean LW CRE (W m^{-2})	101.05	87.24
Mean daily maximum domain-mean LW CRE on rainy days (W m^{-2})	108.57	107.17
Mean daily maximum ice-phase-pixel-mean IWP (g m^{-2})	429.47	277.43
Mean daily maximum ice-phase-pixel-mean IWP on rainy days (g m^{-2})	490.44	388.90

Table 1. SST, Precipitation, LW CRE, and IWP statistics in the El Niño and La Niña winters

Figure 1 shows the probability distributions of the variables of interest and relevant correlations for all of the rainy days. To produce a more normal distribution, we use the $\log_{10}$ of daily accumulated rainfall and daily averaged ice-phase-pixel-mean IWP to create the probability distribution. For rainy days, both daily accumulated rainfall and daily averaged IWP vary by 2-3 orders of magnitude (Figs. 1a and 1d). The large ice cloud mass variation results in a wide LW CRE range from 3.18 to 152.81 W m^{-2} (Fig. 1c). On the daily basis, it does not appear that SST and precipitation have any significant correlation (Fig. 1e). As shown in Fig. 1b, the daily mean SST is always above 301.5 K. The local decoupling between SST and cirrus clouds in the warmest SST regime of the equatorial western Pacific Ocean region was reported in early 1990s (Fu et al. 1992). The zero correlation between SST and precipitation in Fig. 1e also agrees with previous studies showing that the decorrelation between SST and deep convective storms over the entire tropics in this SST range (Lau et al. 1997; Zhang 1993). Daily averaged LW CRE and

precipitation show a weak positive correlation (Fig. 1f), in agreement with the previous study (Zhang et al. 2017). A small positive correlation also exists between daily averaged IWP and precipitation (Fig. 1g). Similarly weak correlations were found between daily maximum LW CRE (LW CREmax) and precipitation, and between daily maximum IWP and precipitation(not shown). Because deep convective cores yield significantly higher precipitation rates than cirrus/ anvil clouds over the tropics (Fu et al. 1990; Schumacher and Houze 2003), the positive correlation between IWP and precipitation on some rainy days in Fig. 1g is expected.

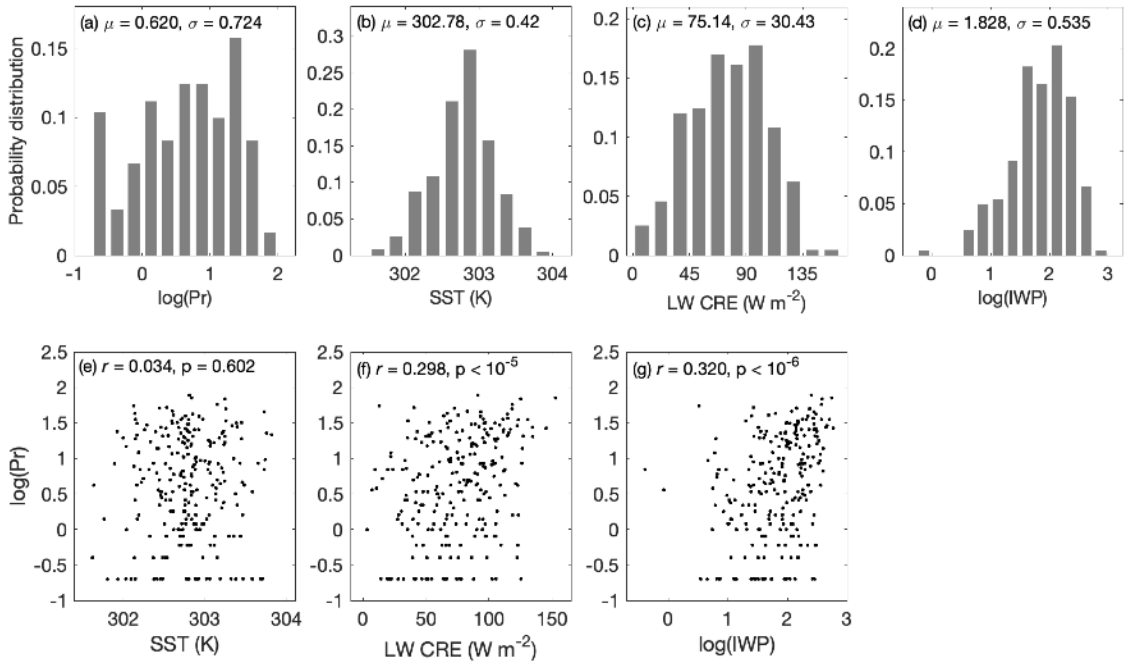

FIG. 1. Probability distributions of (a) logarithm base 10 of daily accumulated rainfall (mm) (log(Pr)), (b) SST (K), (c) daily averaged domain-mean LW CRE (W m^{-2}), and (d) logarithm base 10 of daily averaged ice-phase-pixel-mean IWP on rainy days in the total 4 selected winters and scatterplots of (e) SST vs. log(Pr), (f) LW CRE vs. log(Pr), and (g) log(IWP) vs. log(Pr). In each of the upper panels, μ and σ are the mean and standard deviation of the variable. In each of the lower panels, r and p are the correlation coefficient and p-value of the t-test, respectively.

Overall, the positive correlation between LW CRE and precipitation on the same rainy days is weak, while a moderate positive correlation is observed between LW CRE on a non-rainy day and the precipitation on the subsequent rainy day (Figs. 2a and 2c). In total, 51 non-rainy days followed by rainy days are found during the study period. The moderate positive correlations based on the 51 paired non-rainy–rainy samples in Fig. 2 suggest that if a rainy day is preceded

by a non-rainy day, increased ice clouds with enhanced LW radiative heating of the atmosphere on the non-rainy day often result in enhanced precipitation on the next rainy day over the area of interest. By analyzing spaceborne active and passive observations of clouds and precipitation over global tropical oceans, Masunaga and Bony (2018) showed that cirrus cloud cover above 12 km increases 1-2 days prior to deep convection. Masunaga and Bony (2018) also showed that precipitation associated with deep convection preceded by high cirrus cloudiness is significantly greater than that preceded by low cirrus cloudiness, even though column water vapor contents and SSTs in the high and low cirrus cloudiness conditions are similar. Ren et al. (2020) found that one-layer ice cloud coverage increased up to 5 days before the MJO passage over the Indian Ocean and Maritime Continent. The results shown in Fig. 2 agree with the previous studies (Masunaga and Bony 2018; Ren et al. 2020).

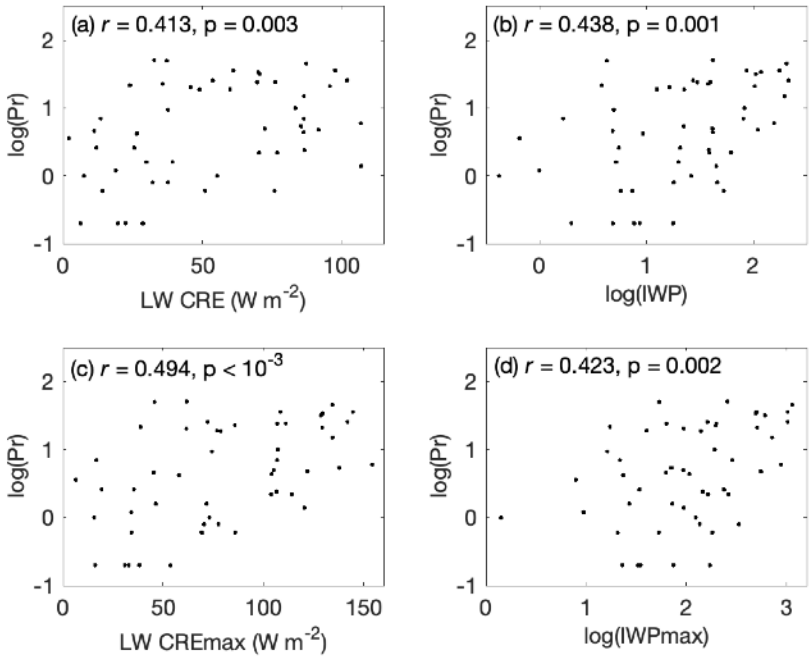

FIG. 2. Scatterplots of (a) log(Pr) vs. LW CRE (W m^{-2}), (b) log(Pr) vs. log(IWP), (c) log(Pr) vs. daily maximum domain-mean LW CRE (LW CREmax; W m^{-2}), and (d) log(Pr) vs. $\log_{10}$ of daily maximum ice-phase-pixel-mean IWP (log(IWPmax)). LW CRE, log(IWP), LW CREmax, and log(IWPmax) are on the non-rainy days, which precede the rainy days by one day. In each panel, *r* and p are the correlation coefficient and *p*-value of the *t*-test, respectively.

b. Thermodynamics revealed by sounding data

The underlying physical processes that link the LW CRE on a rain-free day to the precipitation on the next rainy day may be elucidated with the knowledge of the thermodynamic conditions of the non-rainy–rainy pairs. Figures 3a and 3b show that the day-to-day variation of dry static energy (s) is smaller than the day-to-day variation of MSE (h). As height increases, the standard deviation of s first decreases from near surface to 892.5 hPa and then increases gradually with increasing height. The standard deviations of s at 892.5 and 100 hPa are 0.6 and 2.6 kJ kg^{-1}, respectively. The standard deviation of h shows a minimum of 2.9 kJ kg^{-1} in the lower troposphere at 940 hPa and is below 1.3 kJ kg^{-1} above 255 hPa. In the middle troposphere, the standard deviation of h is 4-5 times larger than that of s, suggesting predominance of humidity variation in determining the h variation. As shown in Fig. 3c, the mean difference between saturated h (h^*) and h within the PBL maximizes at the surface and reaches a minimum around 950 hPa, where the convective cloud base is often found. In the free atmosphere, the mean difference h^*-h maximizes at 760 hPa and decreases above, suggesting that the middle-to-upper troposphere is closer to water vapor saturation than the lower troposphere above PBL. The vertical distribution of h^*-h standard deviation generally follows the vertical distribution of h^*-h mean (Fig. 3c).

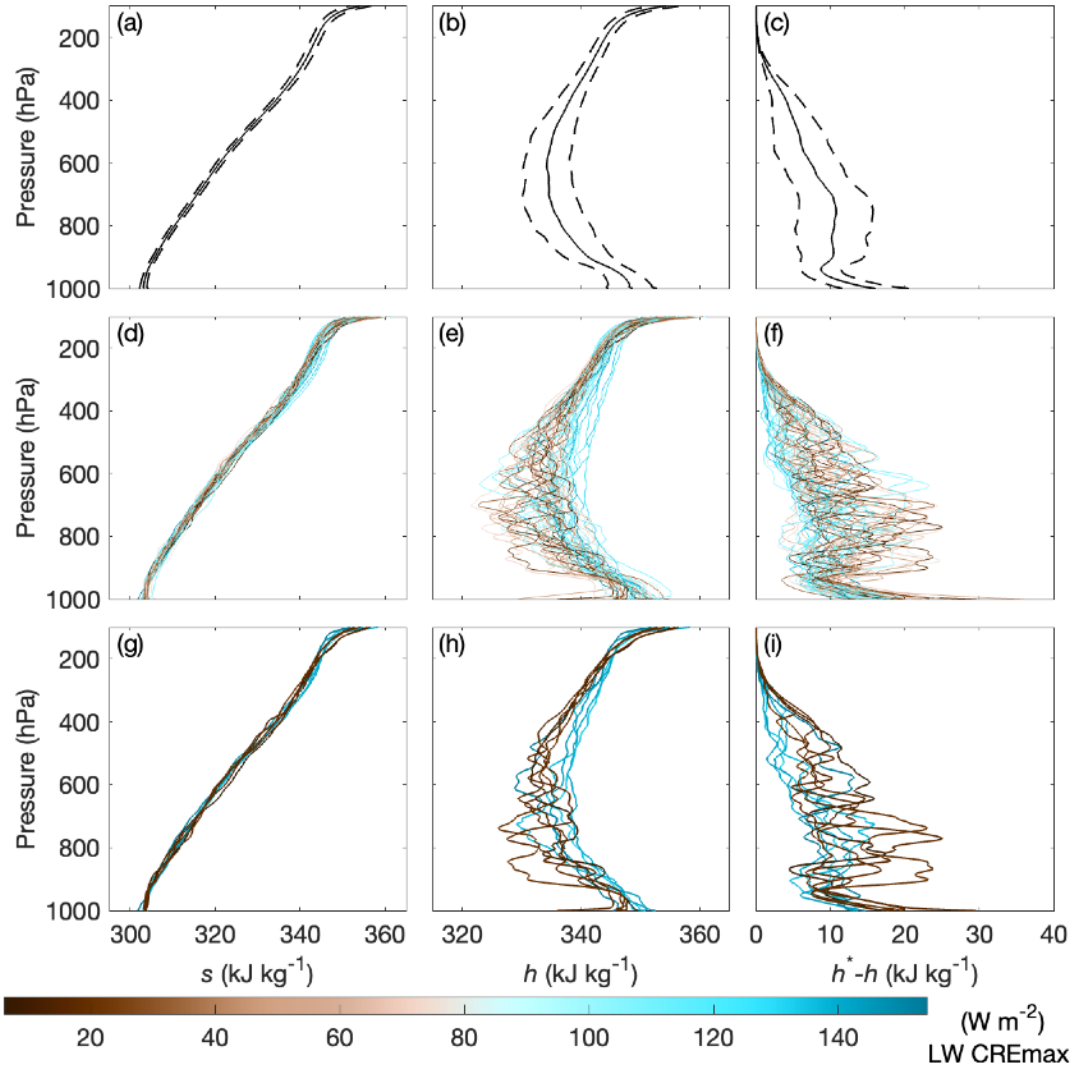

FIG. 3. Vertical profiles of dry static energy (s; kJ kg^{-1}), MSE (h; kJ kg^{-1}), and the difference between saturated MSE (h^*) and MSE (h^*-h; kJ kg^{-1}). The upper panels show the mean and one standard deviation above and below the mean during the entire 4 selected winters. The middle panels show the results on the non-rainy days from the 51 non-rainy–rainy pairs. The lower panels are the same as the middle panels except that only the days with the five largest LW CREmax and the days with the five smallest CREmax are shown. The color of the curves in the middle and lower panels represents the LW CREmax on that day.

Anvil-like clouds dominate the ice cloud population over the equatorial western Pacific (Ren et al. 2021). Deep convective clouds are unlikely to prevail on non-rainy days. Therefore, the observed LW CREs on non-rainy days in this study are probably dominated by anvil clouds. On the non-rainy days followed by rainy days, the 400-200 hPa layer appears to be warmer and the

200-100 hPa layer is cooler when the day has a greater LW CREmax than a smaller LW CREmax (Figs. 3d and 3g). This lower-warming upper-cooling gradient resembles the upper tropospheric vertical LW radiative heating/cooling gradient during the MJO cycle (Ren et al. 2020), owing primarily to ice cloud base absorption and cloud top emission (Fu et al. 1997, 2018). Cloud LW scattering tends to enhance this gradient (Ren et al. 2020). The similarity between the 400–200 hPa warming and 200–100 hPa cooling pattern associated with enhanced LW CRE (Figs. 3g and 3e), and the vertical LW radiative heating/cooling gradient from tropical ice clouds reported by Ren et al. (2020), leads us to hypothesize that enhanced LW CRE due to increased anvil cloud presence on non-rainy days causes the upper-tropospheric vertical warming/cooling gradient observed in this study. In addition, a non-rainy day with enhanced LW CRE shows increased h in the middle-to-upper troposphere between 500 and 200 hPa (Figs. 3e and 3h). Takahashi et al. (2024) found that h increased at those levels across the entire tropics during the two wetter El Niño winters compared to the two La Niña winters. LW radiative heating occurs in the lower portion of anvil-like ice clouds over the equatorial western Pacific while cooling occurs in the upper half of the clouds (Ren et al. 2021). Gu and Liou (2000) used a two-dimensional cirrus cloud model to show that once a cirrus cloud has sufficient water content, LW radiative cooling enhances the ice crystal growth at the cloud top and LW radiative heating enhances the ice crystal sublimation in the lower portion of the cloud. Therefore, the increased h in the middle-to-upper troposphere on non-rainy days found in this study likely results from enhanced ice sublimation, which is facilitated by the LW heating in the lower portion of the cloud. Moreover, h^*-h is also smaller in the middle-to-upper troposphere if a non-rainy day has enhanced LW CRE (Figs. 3f and 3i), suggesting that ice sublimation moistens the middle-to-upper troposphere, approaching water vapor saturation. The moistening at those levels due to ice sublimation enhancement by cloud LW radiative heating shown in Figs. 2 and 3 provides a process-level understanding of the simulated CRE enhancement of the convection-moisture feedback in previous studies (Bony and Emanuel 2005; Grabowski and Moncrieff 2004).

Previous studies showed a close link between atmospheric column-integrated water vapor and precipitation over tropical oceans (Bretherton et al. 2004; Holloway and Neelin 2009). In this study, while the mean h within the PBL on a non-rainy day has the most significant correlation

with rainfall on the subsequent rainy day, mean *h* above the PBL also shows a weak correlation with the rainfall (Figs. 4a-4c). The result agrees with the previous studies that showed the contributions of water vapor in different vertical layers to the precipitation over tropical oceans. In a study from field campaigns in the equatorial Indian Ocean, DePasquale et al. (2014) showed that the troposphere up to 200 hPa was gradually moistened before the MJO onset. Increased upper tropospheric moisture after Kelvin wave passages contributed to the deep tropospheric moisture accumulation (DePasquale et al. 2014). The contrast of the moderate correlation between mean *h* within the PBL and precipitation and the weak correlation between mean *h* in the lower troposphere above the PBL and precipitation (Figs. 4a and 4b) suggests that the PBL moistening is more likely due to increased surface latent heat flux than to entrained moist air from the PBL top. Recalling that SST and precipitation are uncorrelated (Fig. 1e), increased surface evaporation ought to be caused by enhanced surface wind speed, as reported in previous MJO-like disturbance modeling studies (Maloney 2009; Maloney and Sobel 2004; Maloney et al. 2010).

Emanuel (1986) proposed that surface turbulent heat flux plays a dominant role in the intensification and maintenance of tropical cyclones and, more generally, in the development of tropical moist convection. The stronger correlation between *h* within the PBL and precipitation compared to that between *h* in the free atmosphere and precipitation (Figs. 4a-4c) supports that theory. On the other hand, cirrus clouds that carry *h* detrained from tropical deep convection can travel an up to 1000 km long distance before they are dissipated (Luo and Rossow 2004). Convection-generated atmospheric waves are known to help spread anvil clouds (Mapes 1993; Prasad et al. 2019). As shown in Figs. 4d-4f, the most significant correlation between LW CREmax and *h* on non-rainy days is the one between LW CREmax and *h* in the middle-to-upper troposphere ($r = 0.516$). This result further emphasizes that the impact of LW CRE on the thermodynamic condition is primarily due to the LW radiative heating and associated ice sublimation in the lower portion of ice clouds. This finding, along with the previously observed increase in upper-level moisture following Kelvin wave passages during the developing MJO (DePasquale et al. 2014), provides insight in resolving the CQE theory and the criticisms it has faced (Yano and Plant 2012).

The cause and effect relationship between large-scale forcing and deep convection is not clear (Mapes 1993). LW radiative heating/cooling of the atmosphere, a source term of column-integrated h, dominated by the presence of ice clouds, is an order of magnitude smaller than the latent heating generated by tropical deep convection (Masunaga and Bony 2018). Without the deep convection, the ice clouds found on non-rainy days over the study region must arise from somewhere upstream. Thus, in-cloud LW radiative heating of the advecting ice clouds helps heat and moisten the middle-to-upper troposphere and hence regulates the thermodynamic condition for the convection. The impact of tropical deep convection over oceans on the thermodynamics of subsequent convection in the remote region was recognized at least three decades ago (Fu et al. 1996). If the upstream region where ice clouds are generated and the downstream region where subsequent deep convection occurs are studied as a whole, moist convective instability generated by large-scale processes is still possibly balanced by momentum entrainment and frictional drag. Such a modified quasi-equilibrium theory does not ignore convection-generated atmospheric waves. Instead, the modified theory acknowledges that convection-generated atmospheric waves work together with LW CRE to help retain a portion of moisture in the upper levels. With the modified quasi-equilibrium theory, the gap between the moisture mode MJO theory (Adames and Kim 2016) and the gravity wave MJO theory (Yang and Ingersoll 2013), as introduced in Zhang et al. (2020), may also be filled.

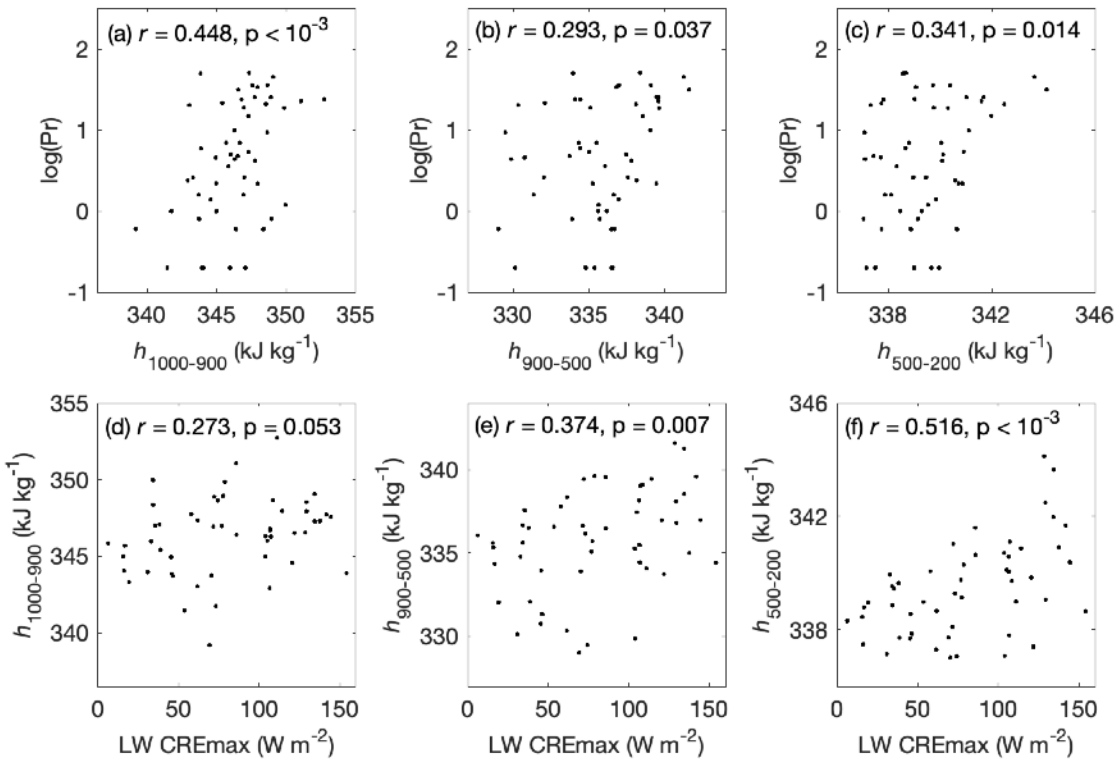

FIG. 4. The upper panels are scatterplots of rainy-day log(Pr) vs. mean MSEs in atmospheric layers between 1000 and 900 hPa ($h_{1000\text{-}900}$; kJ kg^{-1}) (a), between 900 and 500 hPa ($h_{900\text{-}500}$; kJ kg^{-1}) (b), and between 500 and 200 hPa ($h_{500\text{-}200}$; kJ kg^{-1}), respectively. The lower panels are scatterplots of non-rainy day LW CREmax (W m^{-2}) vs. $h_{1000\text{-}900}$, $h_{900\text{-}500}$, and $h_{500\text{-}200}$, respectively. In each panel, r and p are the correlation coefficient and p-value of the t-test, respectively.

In addition, the cloud LW radiative heating enhancement of ice sublimation influences moist convection only if moist convection is going to occur. This conditional influence may help explain why the CRE enhancement of convection-moisture feedback is favorable to tropical oceans and has not been reproduced in studies of storms over midlatitudes (Mischell et al. 2024). While convective instability can be accumulated via the wind feedback and wind-induced surface heat exchange (Emanuel 1987; Neelin et al. 1987) over tropical oceans, the buildup of convective instability over land is controlled by more factors, including large-scale moisture transport, surface solar heating, and soil wetness (Emanuel 2023; Fu et al. 1999). Based on satellite observations, Soden and Fu (1995) showed a positive relationship between the frequency of deep convection and upper-tropospheric humidity at monthly and longer time scales over the tropics. However, they found no correlation between deep convection and upper-level

humidity in extratropical regions. The collocation of enhanced *h* in both lower and upper levels is also important to trigger the so called convective self-aggregation in RCE runs of cloud-permitting models (Held et al. 1993; Wing et al. 2017; Wing et al. 2018). When the cloud ice mixing ratio threshold for cloud ice-to-snow autoconversion is increased from zero to 0.1 g kg^{-1} in a 100-day cloud-permitting simulation, Bretherton et al. (2005) showed that widespread ice cloud development over the dry region slow down the convective self-aggregation in the simulation domain. The convective self-aggregation equivalence in the real atmosphere can be triggered only when enhanced ice sublimation at upper levels and enhanced *h* with the PBL happen simultaneously. Notwithstanding the success that the CQE theory and its variants have received, reaching an equilibrium of a system often consists of several processes operating at different speeds. Unlike middle and high latitudes where convective instability may be accumulated with a large horizontal temperature gradient, low-level humidity often dictates the instability over tropical oceans (Muller et al. 2009). In other words, before the *h* associated with an instability is redistributed or an equilibrium is reached, increased *h* within the PBL usually means increased CAPE over tropical oceans (Raymond 1995).

The same conclusion can be drawn by applying the parcel-lifting theory to the 51 paired non-rainy–rainy samples. As shown in Fig. 5a, lifting condensation level (LCL) on a non-rainy day decreases with increasing rainfall in the next rainy day, although this relationship is weak. This result, at the process level, highlights the importance of surface *h* in determining storm intensity over tropical oceans, as recognized in well-established theories (Emanuel 1995; Raymond 1995). The square root of CAPE ($CAPE^{1/2}$) on a non-rainy day and rainy day precipitation show a very weak correlation (Fig. 5b), less than that between *h* within the PBL and rainfall (Fig. 4a). The result again, at the process level, agrees with the previous theories (Emanuel 1995; Raymond 1995). In agreement with the insignificant correlation between PBL *h* and LW CREmax (Fig. 4d), LCL and LW CREmax are only weakly correlated (Fig. 5c). The in-cloud LW radiative heating enhancement of ice sublimation does not directly influence the humidity within the PBL. Increased humidity in the middle-to-upper troposphere due to ice sublimation reduces the buoyancy of an air parcel pseudo-adiabatically uplifted from the surface to this level. In other words, increased humidity at upper levels reduces CAPE. The insignificant correlation between

$CAPE^{1/2}$ and LW CREmax in Fig. 5d suggests that enhanced ice sublimation in the middle-to-upper troposphere contributes to subsequent rainfall but does not necessarily increase the buoyancy of an air parcel adiabatically rising from the surface. How does increased humidity at upper levels increase the subsequent rainfall amount? Air parcels in convective updrafts are strongly mixed with entrained ambient air in the real atmosphere (Muller et al. 2009). Presumably, the mixing between rising air parcels and the ambient air facilitates the saturation of ambient atmospheric water vapor at upper levels and hence causes increased rainfall.

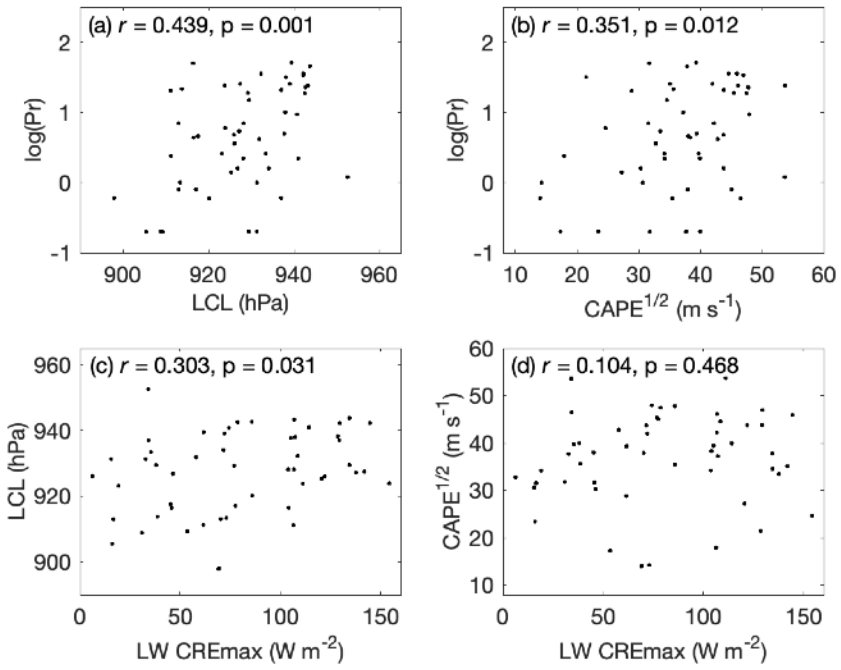

FIG. 5. Scatterplots of (a) log(Pr) vs. lifting condensation level (LCL; hPa), (b) log(Pr) vs. the square root of CAPE ($CAPE^{1/2}$; m s^{-1}), (c) LCL vs. daily maximum domain-mean LW CRE (LW CREmax), and (d) $CAPE^{1/2}$ vs. logarithm base 10 of daily maximum ice-phase-pixel-mean IWP (log(IWPmax)). LCL, $CAPE^{1/2}$, and LW CREmax are on the non-rainy days, which lead the rainy days by one day. In each panel, *r* and p are the correlation coefficient and *p*-value of the *t*-test, respectively.

c. Cloud top temperature and maximum mass temperature

CTT plays an important role in determining the magnitude of the cloud greenhouse effect, leading to extensive study of the relationship between the thermodynamic environment of tropical deep convection and the uppermost detrainment level (Hartmann and Larson 2002; Zelinka and Hartmann 2010, 2011). Figure 6 shows scatterplots of various layer-mean MSEs

and CAPE on non-rainy days versus. daily mean high ice CTT on the following rainy days. While the PBL *h* shows a moderate positive correlation with precipitation (Fig. 4a), no correlation is found between the PBL *h* and CTT (Fig. 6a). No correlation is found between CAPE and CTT either (Fig. 6d). However, *h* in the free atmosphere—particularly in the lower troposphere above the PBL—shows a negative correlation with CTT, although the correlation is very weak (Figs. 6b and 6c). The results suggest that air parcel rising to the cloud top must undergo strong mixing with the ambient air. The more humid the free atmosphere is, the more buoyancy a rising air parcel loses through mixing with the ambient air. From the CQE perspective, the results suggest that enhanced cloud kinetic energy may be balanced by not only an increased cloud top but also increased momentum entrainment. Using cloud-permitting model simulations of tropical deep convection in the RCE, Romps and Kuang (2010) showed that undiluted updrafts are exceedingly rare above approximately 4-5 km and virtually nonexistent above 10 km.

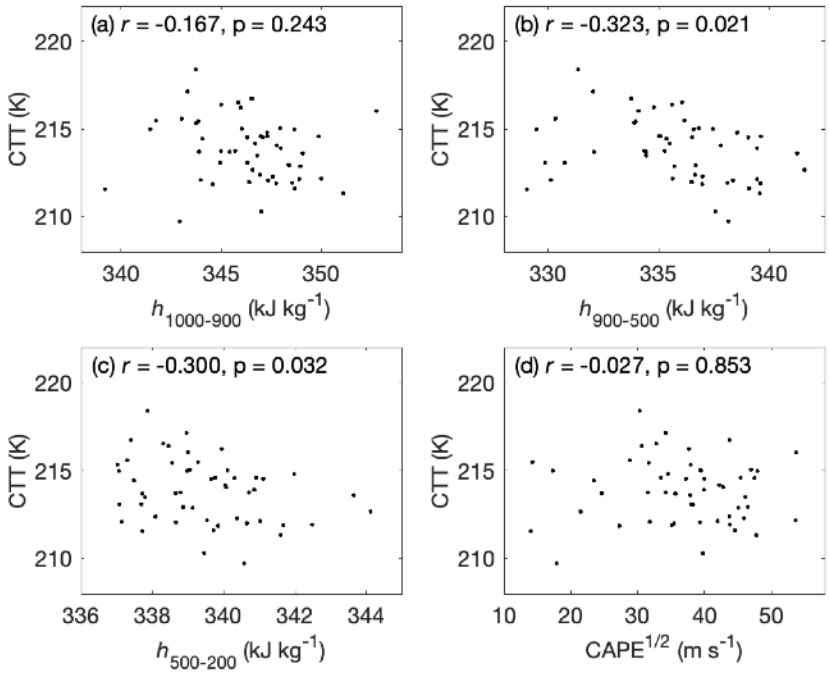

FIG. 6. Scatterplots of daily averaged CERES SYN1deg cloud fraction-weighted mean high ice cloud top temperature (CTT; K) on a rainy day vs. (a) $h_{1000\text{-}900}$, (b) $h_{900\text{-}500}$, (c) $h_{500\text{-}200}$ (kJ kg^{-1}), and (d) CAPE$^{1/2}$ (m s^{-1}) on the previous non-rainy day.

Based on an observed tropical squall line during its intensifying period, detrained solid hydrometeors showed a wide range of vertical distribution between 4–16 km (Mullendore et al. 2009). It was also found that the height at which the anvil ice water content (IWC) maximized was close to the level of maximum detrainment (LMD) 2.5–4 km below the level of neutral buoyancy (LNB) calculated from the nearby sounding data (Mullendore et al. 2009). The LMD is also important to the magnitude of the ice-cloud greenhouse effect (Hartmann and Larson 2002). Because LMD cannot be retrieved from passive sensor observations, active sensor observations are necessary for studying LMD in tropical deep convection (Takahashi and Luo 2012).

Figure 7 compares CERES SYN1deg hourly high ice CTT with coincident CMMT from CloudSat 2C-ICE above 300 hPa. A weak positive correlation is found between CTT and CMMT (Fig. 7). Given that Fig. 6 illustrates the crucial role of mixing between a rising air parcel and the ambient environment in determining CTT, as well as the positive correlation between CTT and CMMT, it is reasonable to expect that both LMD and CMMT are also strongly influenced by this mixing. Based on CPR observations of tropical deep convection, Takahashi and Luo (2012) found only a weak correlation between the conceptually calculated LNB by considering a pseudo-adiabatically rising air parcel and CPR-observed LMD. The discrepancy between the conceptually calculated LNB and the LMD observed by the spaceborne radar serves as a measure of the bulk entrainment rate in convection (Takahashi et al., 2017, 2021). Our results agree with the previous studies. In addition, tropical deep convection has stronger updrafts over land than over ocean (Liu and Zipser 2005). Takahashi and Luo (2012) also showed that while conceptually calculated LNB values are similar between land and ocean, tropical deep convection has a higher LMD over continents and over oceans. Findings from previous studies, along with those of this study, suggest that the humidity of the free atmosphere preceding tropical deep convection plays a crucial role not only in modulating precipitation, but also in determining the altitude at which anvil clouds detrain from deep convective systems. This study further suggests that atmospheric waves generated by deep convection can interact with LW CRE to moisten the upper troposphere ahead of subsequent convection. When deep convection occurs

in a more humid upper troposphere, it tends to produce greater precipitation and lower anvil cloud tops.

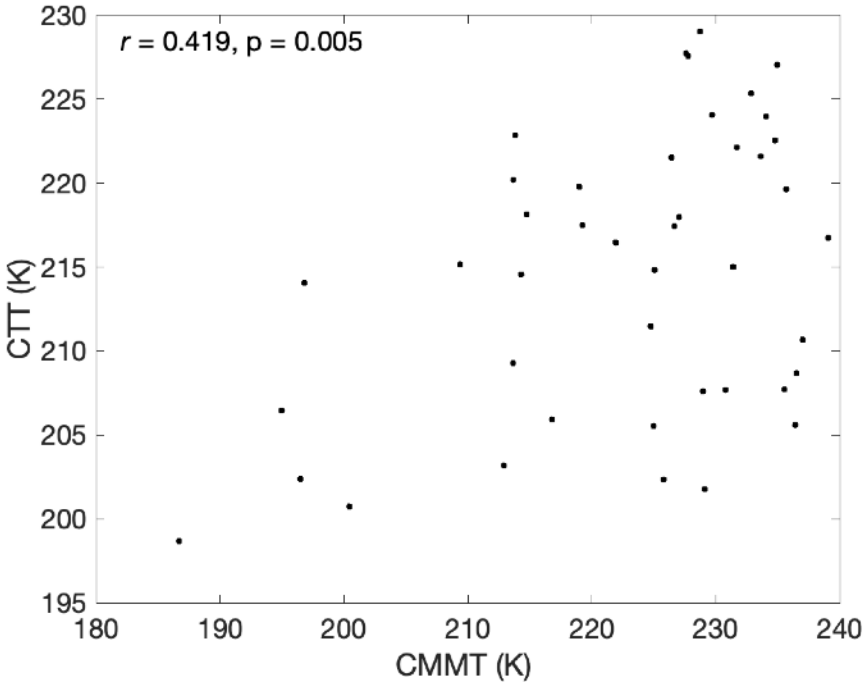

FIG. 7. Scatterplots of CERES SYN1deg hourly high ice CTT (K) vs. CloudSat 2C-ICE above 300 hPa ice cloud maximum mass temperature (CMMT; K) at CloudSat overpasses. Only the cases with more than five 2C-ICE columns that detect ice clouds above 300 hPa but not below over the study domain are included. *r* and p are the correlation coefficient and *p*-value of the *t*-test, respectively.

4. Conclusions

The longwave cloud radiative effect (LW CRE) has been widely studied in relation to tropical moist convection, particularly within the framework of convective quasi-equilibrium (CQE). However, few previous studies have examined the role of LW CRE in the CQE theories from a process-level perspective. This study examined the interplay between precipitation, LW CRE, ice water path (IWP), and moist static energy (MSE) in the tropical western Pacific during El Niño and La Niña winters. On rainy days, weak but positive correlations were found between precipitation and both LW CRE and IWP, consistent with the known link between deep convection and cloud ice mass. More notably, moderate positive correlations emerged between LW CRE and IWP on non-rainy days and precipitation on the following rainy day. This suggests

that enhanced ice clouds and associated LW radiative heating on dry days may precondition the atmosphere for more intense precipitation events.

Sounding data revealed that this preconditioning involves warming in the mid-to-upper troposphere and moistening presumably via ice sublimation driven by LW heating, especially in the lower portions of ice clouds. This radiative process reduces the MSE deficit, bringing the upper troposphere closer to saturation. Stronger correlations between precipitation and MSE within the planetary boundary layer (PBL), as compared to the free troposphere, highlight the critical role of surface latent heat flux—likely wind-driven—in fueling subsequent convection. The atmospheric LW radiative heating by high-level cirrus clouds over tropical oceans is an order of magnitude smaller than the latent heating released from the deep convection that generates the cirrus clouds. However, the present finding helps explain why the greenhouse effect of cirrus clouds is indispensable in the CQE theories which capture important features of tropical moist convection. A recent study shows that including orographic gravity wave parameterization in a GCM enhances the simulated cirrus ice mass over mountainous regions and their downstream areas (Lyu et al. 2023). Based on the findings of this study, we expect that adding convection-generated gravity wave parameterization to a high-resolution global model would significantly enhance the simulated MJO-like disturbance. This enhancement would result from LW radiative heating-facilitated ice sublimation prior to deep convection over tropical oceans. Moreover, we showed that increased humidity in the free atmosphere—particularly in the lower troposphere above the PBL—prior to deep convection tends to lower anvil cloud tops.

Acknowledgement

This study was supported by the NASA Grant 80NSSC22K1890 and partly by the endowment funds (02-512231-00000) associated with the David Bullock Harris Chair in Geosciences at Texas A&M University. We thank Texas A&M High Performance Research Computing (HPRC) for providing the computing resources and software for this study.

Data availability statement

The radiosonde and rain gauge data at the DOE ARM site on the Manus Island, PNG were downloaded from https://adc.arm.gov/discovery/. The ERA5 SST data were downloaded from the Climate Data Store at https://cds.climate.copernicus.eu/datasets/reanalysis-era5-single-levels?tab=overview/. The CERES SYN1deg were accessed from https://ceres.larc.nasa.gov/order_data.php. The CloudSat 2C-ICE data were accessed from the CloudSat Data Processing Center (DPC) at https://www.cloudsat.cira.colostate.edu/.

REFERENCES

Adames, Á. F., and D. Kim, 2016: The MJO as a dispersive, convectively coupled moisture wave: Theory and observations. *J. Atmos. Sci.*, **73,** 913-941, https://doi.org/10.1175/JAS-D-15-0170.1.

Arakawa, A., and W. H. Schubert, 1974: Interaction of a cumulus cloud ensemble with the large-scale environment, Part I. *J. Atmos. Sci.*, **31,** 674-701, https://doi.org/10.1175/1520-0469(1974)031<0674:IOACCE>2.0.CO;2.

Benedict, J. J., B. Medeiros, A. C. Clement, and J. G. Olson, 2020: Investigating the role of cloud-radiation interactions in subseasonal tropical disturbances. *Geophys. Res. Lett.*, **47,** e2019GL086817, https://doi.org/10.1029/2019GL086817.

Bony, S., and K. A. Emanuel, 2005: On the role of moist processes in tropical intraseasonal variability: Cloud–radiation and moisture–convection feedbacks. *J. Atmos. Sci.*, **62,** 2770-2789, https://doi.org/10.1175/JAS3506.1.

Bretherton, C. S., M. E. Peters, and L. E. Back, 2004: Relationships between water vapor path and precipitation over the tropical oceans. *J. Climate*, **17,** 1517-1528, https://doi.org/10.1175/1520-0442(2004)017<1517:RBWVPA>2.0.CO;2.

Bretherton, C. S., P. N. Blossey, and M. Khairoutdinov, 2005: An energy-balance analysis of deep convective self-aggregation above uniform SST. *J. Atmos. Sci.*, **62,** 4273-4292, https://doi.org/10.1175/jas3614.1.

Daloz, A., E. Nelson, T. L'ecuyer, A. Rapp, and L. Sun, 2018: Assessing the coupled influences of clouds on the atmospheric energy and water cycles in reanalyses with A-Train observations. *J. Climate*, **31,** 8241-8264, https://doi.org/10.1175/JCLI-D-17-0862.1.

Deng, M., G. G. Mace, Z. Wang, and H. Okamoto, 2010: Tropical Composition, Cloud and Climate Coupling Experiment validation for cirrus cloud profiling retrieval using CloudSat radar and CALIPSO lidar. *J. Geophys. Res. Atmos.*, **115**, https://doi.org/10.1029/2009JD013104.

Deng, M., G. G. Mace, Z. Wang, and R. P. Lawson, 2013: Evaluation of several A-Train ice cloud retrieval products with in situ measurements collected during the SPARTICUS campaign. *J. Appl. Meteor. Climatol.*, **52,** 1014-1030, https://doi.org/10.1175/JAMC-D-12-054.1.

Deng, M., G. G. Mace, Z. Wang, and E. Berry, 2015: CloudSat 2C-ICE product update with a new Ze parameterization in lidar-only region. *J. Geophys. Res. Atmos.*, **120,** 12,198-112,208, https://doi.org/10.1002/2015JD023600.

DePasquale, A., C. Schumacher, and A. Rapp, 2014: Radar observations of MJO and Kelvin wave interactions during DYNAMO/CINDY2011/AMIE. *J. Geophys. Res. Atmos.*, **119,** 6347-6367, https://doi.org/10.1002/2013JD021031.

Doelling, D. R., M. Sun, L. T. Nguyen, M. L. Nordeen, C. O. Haney, D. F. Keyes, and P. E. Mlynczak, 2016: Advances in geostationary-derived longwave fluxes for the CERES synoptic (SYN1deg) product. *J. Atmos. Ocean. Technol.*, **33,** 503-521, https://doi.org/10.1175/JTECH-D-15-0147.1.

Doelling, D. R., and Coauthors, 2013: Geostationary enhanced temporal interpolation for CERES flux products. *J. Atmos. Ocean. Technol.*, **30,** 1072-1090, https://doi.org/10.1175/JTECH-D-12-00136.1.

Emanuel, K. A., 1986: An air-sea interaction theory for tropical cyclones. Part I: Steady-state maintenance. *J. Atmos. Sci.*, **43,** 585-605, https://doi.org/10.1175/1520-0469(1986)043<0585:AASITF>2.0.CO;2.

——, 1987: An air-sea interaction model of intraseasonal oscillations in the tropics. *J. Atmos. Sci.*, **44,** 2324-2340, https://doi.org/10.1175/1520-0469(1987)044<2324:AASIMO>2.0.CO;2.

——, 1995: The behavior of a simple hurricane model using a convective scheme based on subcloud-layer entropy equilibrium. *J. Atmos. Sci.*, **52,** 3960-3968, https://doi.org/10.1175/1520-0469(1995)052<3960:TBOASH>2.0.CO;2.

——, 2023: On the physics of high CAPE. *J. Atmos. Sci.*, **80,** 2669-2683, https://doi.org/10.1175/JAS-D-23-0060.1.

Fu, Q., M. Smith, and Q. Yang, 2018: The impact of cloud radiative effects on the tropical tropopause layer temperatures. *Atmosphere*, **9,** 377, https://doi.org/10.3390/atmos9100377.

Fu, Q., K. Liou, M. Cribb, T. Charlock, and A. Grossman, 1997: Multiple scattering parameterization in thermal infrared radiative transfer. *J. Atmos. Sci.*, **54,** 2799-2812, https://doi.org/10.1175/1520-0469(1997)054<2799:MSPITI>2.0.CO;2.

Fu, R., A. D. Delgenio, and W. B. Rossow, 1990: Behavior of deep convective clouds in the tropical pacific deduced from ISCCP radiances. *J. Climate*, **3,** 1129-1152, https://doi.org/10.1175/1520-0442(1990)003<1129:bodcci>2.0.co;2.

——, 1994: Influence of ocean surface conditions on atmospheric vertical thermodynamic structure and deep convection. *J. Climate*, **7,** 1092-1108, https://doi.org/10.1175/1520-0442(1994)007<1092:ioosco>2.0.co;2.

Fu, R., W. T. Liu, and R. E. Dickinson, 1996: Response of tropical clouds to the interannual variation of sea surface temperature. *J. Climate*, **9,** 616-634, https://doi.org/10.1175/1520-0442(1996)009<0616:ROTCTT>2.0.CO;2.

Fu, R., B. Zhu, and R. E. Dickinson, 1999: How do atmosphere and land surface influence seasonal changes of convection in the tropical amazon? *J. Climate*, **12,** 1306-1321, https://doi.org/10.1175/1520-0442(1999)012<1306:hdaals>2.0.co;2.

Fu, R., A. D. Delgenio, W. B. Rossow, and W. T. Liu, 1992: Cirrus-cloud thermostat for tropical sea surface temperatures tested using satellite data. *Nature*, **358,** 394-397, https://doi.org/10.1038/358394a0.

Grabowski, W. W., and M. Moncrieff, 2004: Moisture–convection feedback in the tropics. *Quart. J. Roy. Meteor. Soc.*, **130,** 3081-3104, https://doi.org/10.1256/qj.03.135.

Graham, N. E., and T. P. Barnett, 1987: Sea surface temperature, surface wind divergence, and convection over tropical oceans. *Science*, **238,** 657-659, https://doi.org/10.1126/science.238.4827.657.

Gu, B., T. Ren, C.-P. Kuo, P. Yang, and K. Bowman, 2021: Global impact of cloud longwave scattering in an atmosphere-only general circulation model simulation. *J. Geophys. Res. Atmos.*, **126,** e2020JD033968, https://doi.org/10.1029/2020JD033968.

Gu, Y., and K. Liou, 2000: Interactions of radiation, microphysics, and turbulence in the evolution of cirrus clouds. *J. Atmos. Sci.*, **57,** 2463-2479, https://doi.org/10.1175/1520-0469(2000)057<2463:IORMAT>2.0.CO;2.

Hartmann, D. L., and K. Larson, 2002: An important constraint on tropical cloud-climate feedback. *Geophys. Res. Lett.*, **29,** 12-11-12-14, https://doi.org/10.1029/2002GL015835.

Held, I. M., R. S. Hemler, and V. Ramaswamy, 1993: Radiative-convective equilibrium with explicit two-dimensional moist convection. *J. Atmos. Sci.*, **50,** 3909-3927, https://doi.org/10.1175/1520-0469(1993)050<3909:RCEWET>2.0.CO;2.

Hersbach, H., and Coauthors, 2023: ERA5 hourly data on single levels from 1940 to present. Available from: https://doi.org/10.24381/cds.adbb2d47.

Holloway, C. E., and J. D. Neelin, 2009: Moisture vertical structure, column water vapor, and tropical deep convection. *J. Atmos. Sci.*, **66,** 1665-1683, https://doi.org/10.1175/2008JAS2806.1.

Hong, G., 2007: Radar backscattering properties of nonspherical ice crystals at 94 GHz. *J. Geophys. Res. Atmos.*, **112,** D22203, https://doi.org/10.1029/2007JD008839.

Hsiao, W.-T., E. D. Maloney, N. M. Leitmann-Niimi, and C. D. Kummerow, 2024: Observed Relationships between Sea Surface Temperature, Vertical Wind Shear, Tropical Organized Deep Convection, and Radiative Effects. *J. Climate*, **37,** 1277-1293, https://doi.org/10.1175/JCLI-D-23-0262.1.

Jakob, C., M. Singh, and L. Jungandreas, 2019: Radiative convective equilibrium and organized convection: An observational perspective. *J. Geophys. Res. Atmos.*, **124,** 5418-5430, https://doi.org/10.1029/2018JD030092.

Jensen, M., S. Giangrande, T. Fairless, and A. Zhou, 2001: Interpolated Sonde (INTERPOLATEDSONDE). Available from: https://doi.org/10.5439/1095316.

Khairoutdinov, M. F., and K. Emanuel, 2018: Intraseasonal variability in a cloud-permitting near-global equatorial aquaplanet model. *J. Atmos. Sci.*, **75,** 4337-4355, https://doi.org/10.1175/JAS-D-18-0152.1.

Kyrouac, J., Y. Shi, and M. Tuftedal, 1997: Surface Meteorological Instrumentation (MET). Available from: https://doi.org/10.5439/1786358.

Lau, K., H. Wu, and S. Bony, 1997: The role of large-scale atmospheric circulation in the relationship between tropical convection and sea surface temperature. *J. Climate*, **10,** 381-392, https://doi.org/10.1175/1520-0442(1997)010<0381:TROLSA>2.0.CO;2.

Lau, W. K., K.-M. Kim, J.-D. Chern, W.-K. Tao, and L. R. Leung, 2020: Structural changes and variability of the ITCZ induced by radiation–cloud–convection–circulation interactions: inferences from the Goddard Multi-scale Modeling Framework (GMMF) experiments. *Climate Dyn.*, **54,** 211-229, https://doi.org/10.1007/s00382-019-05000-y.

Liu, C. T., and E. J. Zipser, 2005: Global distribution of convection penetrating the tropical tropopause. *J. Geophys. Res. Atmos.*, **110**, https://doi.org/10.1029/2005jd006063.

Lord, S. J., and A. Arakawa, 1980: Interaction of a cumulus cloud ensemble with the large-scale environment. Part II. *J. Atmos. Sci.*, **37,** 2677-2692, https://doi.org/10.1175/1520-0469(1980)037<2677:IOACCE>2.0.CO;2.

Luo, Z., and W. B. Rossow, 2004: Characterizing tropical cirrus life cycle, evolution, and interaction with upper-tropospheric water vapor using Lagrangian trajectory analysis of satellite observations. *J. Climate*, **17,** 4541-4563, https://doi.org/10.1175/3222.1.

Lyu, K., X. Liu, J. Bacmeister, X. Zhao, L. Lin, Y. Shi, and O. Sourdeval, 2023: Orographic cirrus and its radiative forcing in NCAR CAM6. *J. Geophys. Res. Atmos.*, **128,** e2022JD038164, https://doi.org/10.1029/2022JD038164.

Maloney, E. D., 2009: The moist static energy budget of a composite tropical intraseasonal oscillation in a climate model. *J. Climate*, **22,** 711-729, https://doi.org/10.1175/2008JCLI2542.1.

Maloney, E. D., and A. H. Sobel, 2004: Surface fluxes and ocean coupling in the tropical intraseasonal oscillation. *J. Climate*, **17,** 4368-4386, https://doi.org/10.1175/JCLI-3212.1.

Maloney, E. D., A. H. Sobel, and W. M. Hannah, 2010: Intraseasonal variability in an aquaplanet general circulation model. *J. Adv. Model. Earth Syst.*, **2**, https://doi.org/10.3894/JAMES.2010.2.5.

Mapes, B. E., 1993: Gregarious tropical convection. *J. Atmos. Sci.*, **50,** 2026-2037, https://doi.org/10.1175/1520-0469(1993)050<2026:GTC>2.0.CO;2.

Masunaga, H., and S. Bony, 2018: Radiative invigoration of tropical convection by preceding cirrus clouds. *J. Atmos. Sci.*, **75,** 1327-1342, https://doi.org/10.1175/JAS-D-17-0355.1.

Medeiros, B., D. L. Williamson, and J. G. Olson, 2016: Reference aquaplanet climate in the C ommunity A tmosphere M odel, V ersion 5. *J. Adv. Model. Earth Syst.*, **8,** 406-424, https://doi.org/10.1002/2015MS000593.

Medeiros, B., A. C. Clement, J. J. Benedict, and B. Zhang, 2021: Investigating the impact of cloud-radiative feedbacks on tropical precipitation extremes. *npj Climate Atmos. Sci.*, **4,** 18, https://doi.org/10.1038/s41612-021-00174-x.

Middlemas, E. A., A. C. Clement, B. Medeiros, and B. Kirtman, 2019: Cloud radiative feedbacks and El Niño–southern oscillation. *J. Climate*, **32,** 4661-4680, https://doi.org/10.1175/JCLI-D-18-0842.1.

Minnis, P., and Coauthors, 2021: CERES MODIS cloud product retrievals for Edition 4–Part I: Algorithm changes. *IEEE Trans. Geosci. Remote Sens.*, **59**, 2744-2780, https://doi.org/10.1109/TGRS.2020.3008866.

Minnis, P., and Coauthors, 2023: VIIRS Edition 1 cloud properties for CERES, Part 1: Algorithm adjustments and results. *Remote Sens*., **15**, 578, https://doi.org/10.1109/10.3390/rs15030578.

Mischell, E., B. Soden, B. Zhang, T. L. Hsieh, and G. Vecchi, 2024: Why does atmospheric radiative heating weaken midlatitude cyclones? *Geophys. Res. Lett.*, **51,** e2024GL110754, https://doi.org/10.1029/2024GL110754.

Mullendore, G. L., A. J. Homann, K. Bevers, and C. Schumacher, 2009: Radar reflectivity as a proxy for convective mass transport. *J. Geophys. Res. Atmos.*, **114**, https://doi.org/10.1029/2008JD011431.

Muller, C. J., L. E. Back, P. A. O'Gorman, and K. A. Emanuel, 2009: A model for the relationship between tropical precipitation and column water vapor. *Geophys. Res. Lett.*, **36**, https://doi.org/10.1029/2009GL039667.

Neelin, J. D., and I. M. Held, 1987: Modeling tropical convergence based on the moist static energy budget. *Mon. Wea. Rev.*, **115,** 3-12, https://doi.org/10.1175/1520-0493(1987)115<0003:MTCBOT>2.0.CO;2.

Neelin, J. D., I. M. Held, and K. H. Cook, 1987: Evaporation-wind feedback and low-frequency variability in the tropical atmosphere. *J. Atmos. Sci.*, **44,** 2341-2348, https://doi.org/10.1175/1520-0469(1987)044<2341:EWFALF>2.0.CO;2.

Prasad, A. A., S. C. Sherwood, M. J. Reeder, and T. P. Lane, 2019: Rapidly evolving cirrus clouds modulated by convectively generated gravity waves. *J. Geophys. Res. Atmos.*, **124,** 7327-7338, https://doi.org/10.1029/2019JD030538.

Ramanathan, V., 1987: The role of earth radiation budget studies in climate and general circulation research. *J. Geophys. Res. Atmos.*, **92,** 4075-4095, https://doi.org/10.1029/JD092iD04p04075.

Raymond, D. J., 1995: Regulation of moist convection over the west Pacific warm pool. *J. Atmos. Sci.*, **52,** 3945-3959, https://doi.org/10.1175/1520-0469(1995)052<3945:ROMCOT>2.0.CO;2.

——, 2000: The Hadley circulation as a radiative–convective instability. *J. Atmos. Sci.*, **57,** 1286-1297, https://doi.org/10.1175/1520-0469(2000)057<1286:THCAAR>2.0.CO;2.

Ren, T., D. Li, J. Muller, and P. Yang, 2021: Sensitivity of radiative flux simulations to ice cloud parameterization over the equatorial western Pacific Ocean region. *J. Atmos. Sci.*, **78,** 2549-2571, https://doi.org/10.1175/JAS-D-21-0017.1.

Ren, T., P. Yang, C. Schumacher, X. Huang, and W. Lin, 2020: Impact of cloud longwave scattering on radiative fluxes associated with the Madden-Julian Oscillation in the Indian Ocean and Maritime Continent. *J. Geophys. Res. Atmos.*, **125,** e2020JD032591, https://doi.org/10.1029/2020JD032591.

Romps, D. M., and Z. Kuang, 2010: Do undiluted convective plumes exist in the upper tropical troposphere? *J. Atmos. Sci.*, **67,** 468-484, https://doi.org/10.1175/2009JAS3184.1.

Schäfer, S. A., and A. Voigt, 2018: Radiation weakens idealized midlatitude cyclones. *Geophys. Res. Lett.*, **45,** 2833-2841, https://doi.org/10.1002/2017GL076726.

Schumacher, C., and R. A. Houze Jr, 2003: Stratiform rain in the tropics as seen by the TRMM precipitation radar. *J. Climate*, **16,** 1739-1756

Sherwood, S. C., V. Ramanathan, T. P. Barnett, M. K. Tyree, and E. Roeckner, 1994: Response of an atmospheric general circulation model to radiative forcing of tropical clouds. *J. Geophys. Res. Atmos.*, **99,** 20829-20845, https://doi.org/10.1029/94JD01632.

Slingo, A., and J. Slingo, 1988: The response of a general circulation model to cloud longwave radiative forcing. I: Introduction and initial experiments. *Quart. J. Roy. Meteor. Soc.*, **114,** 1027-1062, https://doi.org/10.1002/qj.49711448209.

Slingo, J., and A. Slingo, 1991: The response of a general circulation model to cloud longwave radiative forcing. II: Further studies. *Quart. J. Roy. Meteor. Soc.*, **117,** 333-364, https://doi.org/10.1002/qj.49711749805.

Soden, B. J., and R. Fu, 1995: A satellite analysis of deep convection, upper-tropospheric humidity, and the greenhouse effect. *J. Climate*, **8,** 2333-2351, https://doi.org/10.1175/1520-0442(1995)008<2333:ASAODC>2.0.CO;2.

Sun, L., A. Rapp, T. L'Ecuyer, A. Daloz, and E. Nelson, 2022: Environmental response in coupled energy and water cloud impact parameters derived from A-Train satellite, ERA-Interim and MERRA-2. *J. Appl. Meteor. Climatol.*, **61,** 261-276, https://doi.org/10.1175/JAMC-D-21-0078.1.

Sun-Mack, S., P. Minnis, Y. Chen, G. Hong, and W. L. Smith, Jr., 2024: Identification of ice-over-water multilayer clouds using multispectral satellite data in an artificial neural network. *Atmos. Meas. Tech.*, **17**, 3323–3346, https://doi.org/10.5194/amt-17-3323-2024.

Takahashi, H., and Z. Luo, 2012: Where is the level of neutral buoyancy for deep convection? *Geophys. Res. Lett.*, **39**, https://doi.org/10.1029/2012GL052638.

Takahashi, H., Z. J. Luo, and G. L. Stephens, 2017: Level of neutral buoyancy, deep convective outflow, and convective core: New perspectives based on 5 years of CloudSat data. *J. Geophys. Res. Atmos.*, **122,** 2958-2969, https://doi.org/10.1002/2016JD025969.

Takahashi, H., Z. J. Luo, and G. Stephens, 2021: Revisiting the entrainment relationship of convective plumes: A perspective from global observations. *Geophys. Res. Lett.*, **48,** e2020GL092349, https://doi.org/10.1029/2020GL092349.

Takahashi, H., Z. J. Luo, H. Masunaga, R. Storer, and A. T. Noda, 2024: Investigating convective processes underlying ENSO: New insights into the fixed anvil temperature hypothesis. *Geophys. Res. Lett.*, **51,** e2023GL107113, https://doi.org/10.1029/2023GL107113.

Tanelli, S., and Coauthors, 2008: CloudSat's cloud profiling radar after two years in orbit: Performance, calibration, and processing. *IEEE Trans. Geosci. Remote Sens.*, **46,** 3560-3573, https://doi.org/10.1109/TGRS.2008.2002030.

Tian, B., and V. Ramanathan, 2002: Role of tropical clouds in surface and atmospheric energy budget. *J. Climate*, **15,** 296-305, https://doi.org/10.1175/1520-0442(2002)015<0296:ROTCIS>2.0.CO;2.

——, 2003: A simple moist tropical atmosphere model: The role of cloud radiative forcing. *J. Climate*, **16,** 2086-2092, https://doi.org/10.1175/1520-0442(2003)016<2086:ASMTAM>2.0.CO;2.

Trepte, Q. Z., and Coauthors, 2019: Global cloud detection for CERES Edition 4 using Terra and Aqua MODIS data. *IEEE Trans. Geosci. Remote Sens.*, **57**, 9410-9449, https://doi.org/10.1109/TGRS.2019.2926620.

Wall, C. J., D. L. Hartmann, M. M. Thieman, W. L. Smith, Jr., and P. Minnis, 2018: The life cycle of anvil clouds and the top-of-atmosphere radiation balance over the tropical West Pacific. *J. Climate*, **31**, 10059-10080, https://doi.org/10.1175/JCLI-D-18-0154.1.

Wing, A. A., K. Emanuel, C. E. Holloway, and C. Muller, 2017: Convective self-aggregation in numerical simulations: a review. *Surv. Geophys.*, **38,** 1173-1197, https://doi.org/10.1007/s10712-017-9408-4.

Wing, A. A., K. A. Reed, M. Satoh, B. Stevens, S. Bony, and T. Ohno, 2018: Radiative–convective equilibrium model intercomparison project. *Geosci. Model Dev.*, **11,** 793-813, https://doi.org/10.5194/gmd-11-793-2018.

Winker, D., and Coauthors, 2010: The CALIPSO mission: A global 3D view of aerosols and clouds. *Bull. Amer. Meteor. Soc.*, **91,** 1211-1229, https://doi.org/10.1175/2010BAMS3009.1.

Xu, K.-M., and K. A. Emanuel, 1989: Is the tropical atmosphere conditionally unstable? *Mon. Wea. Rev.*, **117,** 1471-1479, https://doi.org/10.1175/1520-0493(1989)117<1471:ITTACU>2.0.CO;2.

Xu, K.-M., T. Wong, B. A. Wielicki, L. Parker, and Z. A. Eitzen, 2005: Statistical analyses of satellite cloud object data from CERES. Part I: Methodology and preliminary results of the 1998 El Niño/2000 La Niña. *J. Climate*, **18,** 2497-2514, https://doi.org/10.1175/JCLI3418.1.

Xu, K.-M., T. Wong, B. A. Wielicki, L. Parker, B. Lin, Z. A. Eitzen, and M. Branson, 2007: Statistical analyses of satellite cloud object data from CERES. Part II: Tropical convective cloud objects during 1998 El Niño and evidence for supporting the fixed anvil temperature hypothesis. *J. Climate*, **20,** 819-842, https://doi.org/10.1175/JCLI4069.1.

Xu, K. M., Y. Hu, and T. Wong, 2019: Convective aggregation and indices examined from CERES cloud object data. *J. Geophys. Res. Atmos.*, **124,** 13604-13624, https://doi.org/10.1029/2019JD030816.

Yang, D., and A. P. Ingersoll, 2013: Triggered convection, gravity waves, and the MJO: A shallow-water model. *J. Atmos. Sci.*, **70,** 2476-2486, https://doi.org/10.1175/JAS-D-12-0255.1.

Yang, P., K. Liou, K. Wyser, and D. Mitchell, 2000: Parameterization of the scattering and absorption properties of individual ice crystals. *J. Geophys. Res. Atmos.*, **105,** 4699-4718, https://doi.org/10.1029/1999JD900755.

Yano, J. I., and R. Plant, 2012: Convective quasi-equilibrium. *Rev. Geophys.*, **50**, https://doi.org/10.1029/2011RG000378.

Zelinka, M. D., and D. L. Hartmann, 2010: Why is longwave cloud feedback positive? *J. Geophys. Res. Atmos.*, **115,** D16117, https://doi.org/10.1029/2010JD013817.

——, 2011: The observed sensitivity of high clouds to mean surface temperature anomalies in the tropics. *J. Geophys. Res. Atmos.*, **116**, https://doi.org/10.1029/2011JD016459.

Zhang, B., R. J. Kramer, and B. J. Soden, 2019: Radiative feedbacks associated with the Madden–Julian Oscillation. *J. Climate*, **32,** 7055-7065, https://doi.org/10.1175/JCLI-D-19-0144.1.

Zhang, B., B. J. Soden, and G. A. Vecchi, 2023: A vertically resolved analysis of radiative feedbacks on moist static energy variance in tropical cyclones. *J. Climate*, **36,** 1125-1141, https://doi.org/10.1175/JCLI-D-22-0199.1.

Zhang, B., B. J. Soden, G. A. Vecchi, and W. Yang, 2021a: Investigating the causes and impacts of convective aggregation in a high resolution atmospheric GCM. *J. Adv. Model. Earth Syst.*, **13,** e2021MS002675, https://doi.org/10.1029/2021MS002675.

——, 2021b: The role of radiative interactions in tropical cyclone development under realistic boundary conditions. *J. Climate*, **34,** 2079-2091, https://doi.org/10.1175/JCLI-D-20-0574.1.

Zhang, C., 1993: Large-scale variability of atmospheric deep convection in relation to sea surface temperature in the tropics. *J. Climate*, **6,** 1898-1913

Zhang, C., Á. Adames, B. Khouider, B. Wang, and D. Yang, 2020: Four theories of the Madden-Julian Oscillation. *Rev. Geophys.***,** e2019RG000685, https://doi.org/10.1029/2019RG000685.

Zhang, K., W. J. Randel, and R. Fu, 2017: Relationships between outgoing longwave radiation and diabatic heating in reanalyses. *Climate Dyn.*, **49,** 2911-2929, https://doi.org/10.1007/s00382-016-3501-0.